Journal of Materials Chemistry A

PAPER

View Article Online
View Journal | View Issue

Cite this: J. Mater. Chem. A, 2018, 6, 14797

Sandwich-like CNTs/Si/C nanotubes as high performance anode materials for lithium-ion batteries†

Ruiping Liu,*[abc] Chao Shen,[a] Yue Dong,[a] Jinlei Qin,[a] Qi Wang,[a] James Iocozzia,[c] Shiqiang Zhao,[c] Kunjie Yuan,[c] Cuiping Han,[d] Baohua Li[e] and Zhiqun Lin*[c]

Received 20th May 2018
Accepted 4th July 2018

DOI: 10.1039/c8ta04686g

rsc.li/materials-a

Co-axial silicon-coated carbon nanotubes (CNTs/Si) were successfully synthesized *via* a hydrothermal method. Sandwich-like carbon-coated CNTs/Si were obtained by an additional carbon coating. The as-prepared materials show superior cycling performance as anode materials in lithium ion batteries with a current density as high as 500 mA g^{-1} with no observable structural changes during the charge/discharge process. In addition, stable reversible discharge capacities as high as 1508.5 mA h g^{-1} after 1000 cycles were obtained. At higher current densities of 1 A g^{-1} and 2 A g^{-1}, the CNTs/Si/C nanotubes also showed ideal cycling performance with reversible discharge capacities of 1216.6 mA h g^{-1} and 932.2 mA h g^{-1}, respectively. The sandwich-like hollow tube structure of CNTs/Si/C not only alleviates the volume change during cycling, but also facilitates Li-ion and electron transport, and stabilizes the SEI layer. These results suggest that sandwich-like CNTs/Si/C nanotubes are a promising anode material for lithium ion batteries.

Introduction

With the wide application of portable electric devices, electric vehicles and hybrid electric vehicles, new energy storage materials with both high energy density and high power density are highly required.[1,2] Among various energy storage methods, lithium ion batteries have attracted much attention due to their high energy density, high power density, high output voltage, low environmental impact and long cycle life.[3,4] It is well known that the energy density of batteries is heavily dependent on the cathode and anode materials. Unfortunately, due to its relatively low theoretical capacity (372 mA h g^{-1}) and safety concerns associated with lithium plating and lithium dendrite formation, the current commercially available graphite-based anodes cannot meet the increasing demands for energy density and reliability necessary for portable electronic devices and electric vehicles.[5–7] Therefore, it is essential to develop new anode materials with higher theoretical capacities to replace graphite-based materials.

Among various candidate anodes materials, silicon-based materials are the most promising due to their low cost, environmental friendliness, non-toxicity, and high theoretical capacity of 4200 mA h g^{-1} (when fully lithiated to $Li_{4.4}Si$), more than 10 times that of carbonaceous materials.[8,9] However, Si anodes also suffer from several major drawbacks that have greatly limited their development. The primary challenge with Si anodes comes from the large volume change during the charge/discharge process (~400%) associated with lithium ion intercalation and de-intercalation. This large volume change leads the pulverization of the electrodes and instability of the solid electrolyte interphase (SEI). Over time, the active materials may also peel off from the current collector, resulting in poor cycling stability of the batteries. In addition, the poor intrinsic electrical conductivity of Si-based materials contributes to sluggish electrochemical kinetics, particularly at higher cycling rates, which has limited their use at high current densities (*i.e.* fast charging).[10–13]

Much effort has been devoted to addressing the above problems. For example, it has been reported that decreasing the size of Si to the nanoscale and introducing pores into Si-based materials are two effective strategies for accommodating the volume change during the charge/discharge processes and limiting the pulverization of Si anodes. Expanding on the above strategies, Si-based anode materials with various

[a]Department of Materials Science and Engineering, China University of Mining & Technology (Beijing), Beijing 100083, China. E-mail: bjlrp165@126.com; Fax: +86 10-62339081; Tel: +86 10-62339175

[b]State Key Laboratory of Coal Resources and Safe Mining, China University of Mining & Technology (Beijing), Beijing 100083, China

[c]School of Materials Science and Engineering, Georgia Institute of Technology, Atlanta, GA 30332, USA. E-mail: zhiqun.lin@mse.gatech.edu; Fax: +1-404-385-3734; Tel: +1-404-385-4404

[d]College of Materials Science and Engineering, Shenzhen University, Shenzhen Key Laboratory of Special Functional Materials, Shenzhen 518060, China

[e]Engineering Laboratory for Next Generation Power and Energy Storage Batteries, Graduate School at Shenzhen, Tsinghua University, Shenzhen 518055, China

† Electronic supplementary information (ESI) available. See DOI: 10.1039/c8ta04686g

nanostructures such as nanoparticles,[14–16] nanospheres,[17,18] nanowires[19] and nanotube arrays[20,21] have been synthesized and applied for use in lithium ion batteries. Concurrently, carbon-containing materials have been combined with Si to form hybrid materials for improved anode electrical conductivity. These strategies have led to enhanced electrochemical performance in lithium ion batteries.[22,23]

One dimensional (1D) Si nanotubes can develop hoop stress/strain relaxation during the charge/discharge processes by reducing the shell thickness to a few nanometers. This behavior may be beneficial for Li^+ and the electron transport process due to the reduced diffusion path, potentially leading to improved rate and cycling performance of Si-based anodes. Thus by transitioning from nanoparticles (0D) to nanotubes (1D), many of the problems associated with Si anode materials can be reduced. However, the fabrication of these 1D Si nanotubes commonly requires a metal oxide template such as MgO, ZnO or AAO. Si is deposited by a CVD or sol–gel method with subsequent removal of the template to obtain Si nanotubes. This synthesis method suffers from complex procedures, high costs, and the use of toxic precursors.[24–28] Carbon nanotubes (CNTs) with excellent mechanical and electrical properties can enhance the electrical conductivity and serve as a structure stabilizer during the charge/discharge process. CNTs may also be ideal templates for the deposition of Si nanotubes. Herein, we report a facile hydrothermal method for synthesizing core–shell CNTs/SiO_2 intermediates, in which the SiO_2 is reduced to Si and coated with carbon to obtain sandwich-like coaxial core–shell CNTs/Si/C. The resulting nanostructured material had superior cycling performance with no observable damage even after 1000 cycles at current densities of 1 A g^{-1} and 2 A g^{-1}. CNTs/Si/C anodes also showed improved rate performance in lithium ion batteries.

Results and discussion

The step-by-step synthesis and the growth process of CNTs/Si/C nanotubes are illustrated in Fig. 1 and S1,† respectively. CNTs were employed as the template for the selective heterogeneous nucleation and growth of a thin layer of silica under hydrothermal conditions using tetraethyl orthosilicate (TEOS) as the silica source (Fig. S1†). Next, magnesiothermic reduction method was applied to convert the SiO_2 shell into Si at 750 °C after 4 h under an Ar atmosphere. Pure CNTs/Si can be obtained by etching the reduction product (MgO) and the unreacted SiO_2 in HCl and HF, respectively. The obtained CNTs/Si can be directly treated with a Tris buffer solution containing dopamine and calcined to obtain CNTs/Si/C.

The morphologies of the as-prepared Si nanotube composites are shown in Fig. 2. TEOS was hydrolyzed under alkaline conditions and bonded to carbon nanotubes in the presence of hexadecyltrimethylammonium bromide (CTAB), yielding a uniform and complete SiO_2 layer over CNTs after hydrothermal treatment (Fig. 2(a)). After reduction, the formed CNTs/Si also decreased in diameter (Fig. 2(b) and (f)). The sandwich-like CNTs/Si/C nanotubes were synthesized after coating a thin carbon layer on the outer surface of the CNTs/Si (Fig. 2(d)). In order to confirm the formation of Si nanotubes, the pure Si nanotubes were obtained by removing CNTs, as shown in Fig. 2(c) and (e). TEM analysis further confirmed that highly crystalline Si layers were uniformly coated on the surface of the CNTs after magnesiothermic reduction of SiO_2, with a thickness of around 10 nm. A thin carbon layer with a thickness of 2–3 nm deposited on the surface of the Si nanotubes can also be seen (Fig. 2(g)). TEM of the CNTs/Si/C clearly confirms the hollow characteristic of the nanostructure. And the HRTEM image shows that the silicon is well crystallized, and the lattice fringes with a spacing of 0.31 nm can be indexed to the Si (111) lattice planes (Fig. 2(h)).

The phase composition of the samples was determined by XRD and XPS, as shown in Fig. 3. The CNTs/Si were obtained by a hydrothermal process, and after complete reduction of silica and removal of the CNTs by calcination, the characteristic peaks of Si at 28°, 47°, 57°, and 76° were clearly observed in the XRD pattern, indicating the presence of pure silicon nanotubes. The calculated Si crystal size from the XRD peak is approximately 2.7 nm (Fig. 3(a)). The XPS spectra show a Si 2p peak (composed of $2p_{3/2}$ and $2p_{1/2}$ due to spin–orbit coupling) attributed to bulk silicon (~99.5 eV) (Fig. 3(b)). Furthermore, the EDS (Fig. S2†) and Raman (Fig. S3†) spectra confirm that the Si nanotubes were successfully prepared, in agreement with the TEM, EDS and Raman results. The nitrogen adsorption–desorption isotherm shows an obvious hysteresis loop at higher relative pressure, which indicates the presence of mesopores[29,30] (Fig. S4†). The Brunauer–Emmett–Teller (BET) specific surface area is 84.58 m^2 g^{-1}. The hierarchical pores with mean pore sizes of 4.9 nm and 17.8 nm can be detected, which originated from the silicon wall and the CNTs, respectively (the inset of Fig. S4†). The TG curve (Fig. S5†) shows that the content of Si of the sandwich-like CNTs/Si/C nanotubes is about 70%, which can guarantee the energy density of the Li-ion batteries.

In order to evaluate the electrochemical performance of the CNTs/Si/C anodes in lithium ion batteries, the half-cell was

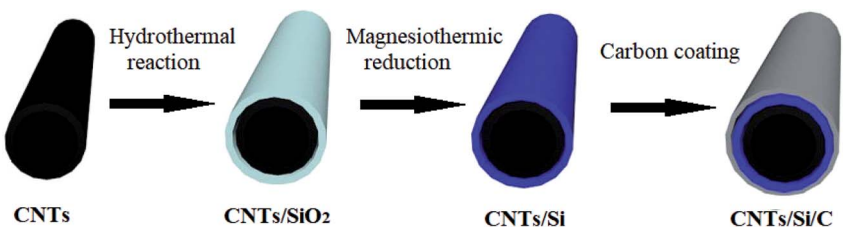

Fig. 1 Schematic illustration of the CNT-templated formation of CNTs/Si/C composites.

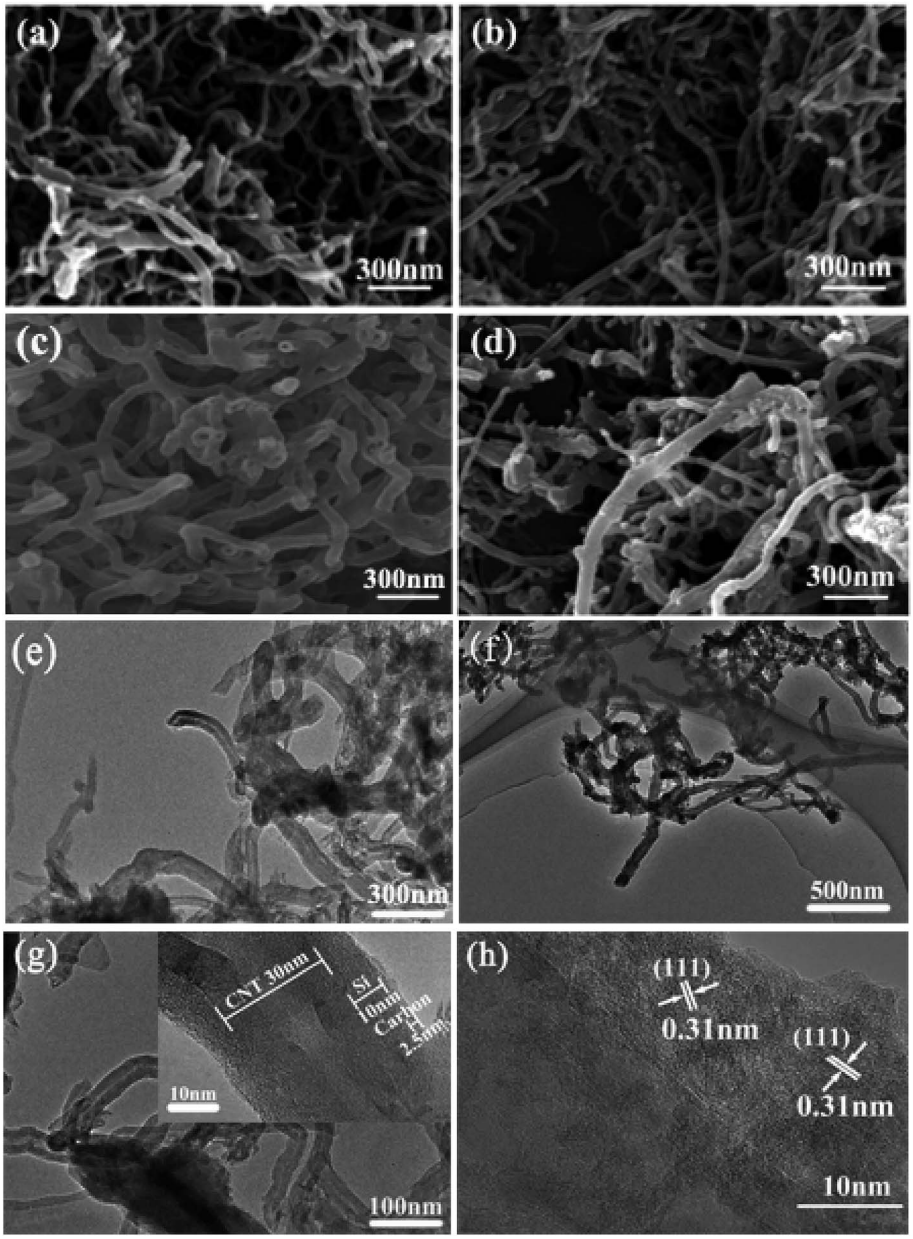

Fig. 2 SEM images of (a) CNTs/SiO_2, (b) CNTs/Si, (c) Si nanotubes and (d) CNTs/Si/C. TEM images of (e) Si nanotubes, (f) CNTs/Si, and (g–h) CNTs/Si/C.

subjected to cyclic voltammetry (CV) tests. Fig. S6† shows the CV of the cells with CNTs/Si/C nanotubes as anode materials at a scan rate of 0.1 mV s^{-1} from 0.0 to 2.0 V. It can be seen that the first charge–discharge curve is different from others, indicating the irreversible reaction occurring during the process. During the first cycle, the sharp negative peak at 0.65 V *vs.* Li/Li^+ is attributed to the formation of a SEI layer, which disappears in the subsequent cycles. The reduction peak at 0.15 V can be attributed to the formation of a Li–Si alloy. As for the discharge process, two distinct peaks located at 0.33 V and 0.48 V in the first cycle correspond to the lithiation process. After the first cycle, the anodic peak potential of the electrode shifts to the higher voltage region. This suggests reduced anode polarization and increased Li^+ insertion/extraction reversibility during electrochemical cycling.

Fig. 4(a–c) show the cycle performance of the prepared anode materials. It can be seen that CNTs/Si deliver initial charge and discharge capacities of 758.4 and 1520 mA h g^{-1} at a current density of 500 mA g^{-1}, with an initial coulombic efficiency of 49.9%. The discharge capacity decreases to 584 mA h g^{-1} in the first 50 cycles, and then increases gradually to 1284 mA h g^{-1} after 1000 cycles. This indicates that the CNTs/Si anodes undergo an initial activation process.[31,32] Compared to the CNTs/Si, the CNTs/Si/C nanotubes show relatively smooth charge/discharge curves and higher capacities. At a current density of 500 mA g^{-1}, the initial charge and discharge

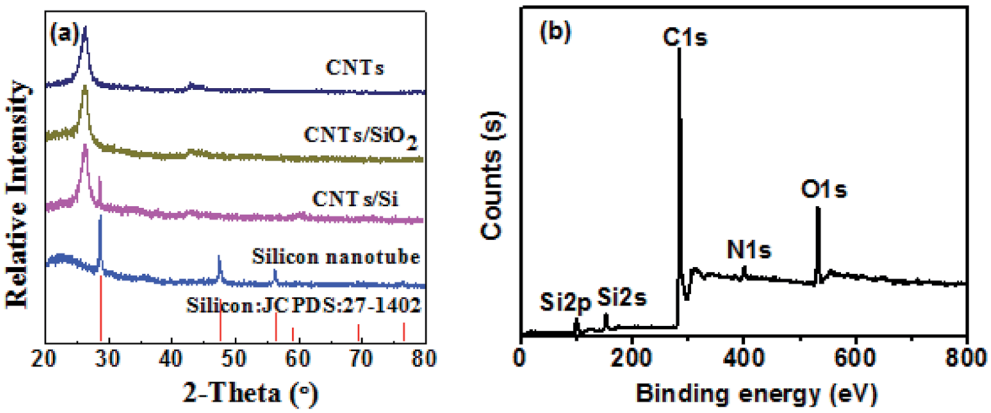

Fig. 3 (a) XRD pattern and (b) XPS spectrum of the CNTs/Si/C nanotubes.

capacities of CNTs/Si/C nanotubes are 1280.4 and 1933.6 mA h g^{-1}, respectively, with an initial coulombic efficiency of 66.2%. After decreasing to 1180.7 mA h g^{-1} within the first 30 cycles, the discharge capacity gradually increased to 1508.5 mA h g^{-1} after 1000 cycles. The irreversible capacity loss of the first discharge–charge process can be attributed to the formation of a solid electrolyte interphase (SEI) layer *via* electrolyte decomposition and trapped Li^+ inserted into the abundant inner pores of the CNTs/Si/C nanotubes. Furthermore, at higher current densities of 1 A g^{-1} and 2 A g^{-1}, the initial discharge capacities of CNTs/Si/C nanotubes are 1822.6 and 1433.8 mA h g^{-1}. After 1000 cycles, discharge capacities of 1216.6 and 932.2 mA h g^{-1} can be restored, indicating improved cycling performance for the CNTs/Si/C nanotubes. It is worth noting that the discharge capacity of the CNTs/Si/C nanotubes increased with increasing cycles, with this most apparent at

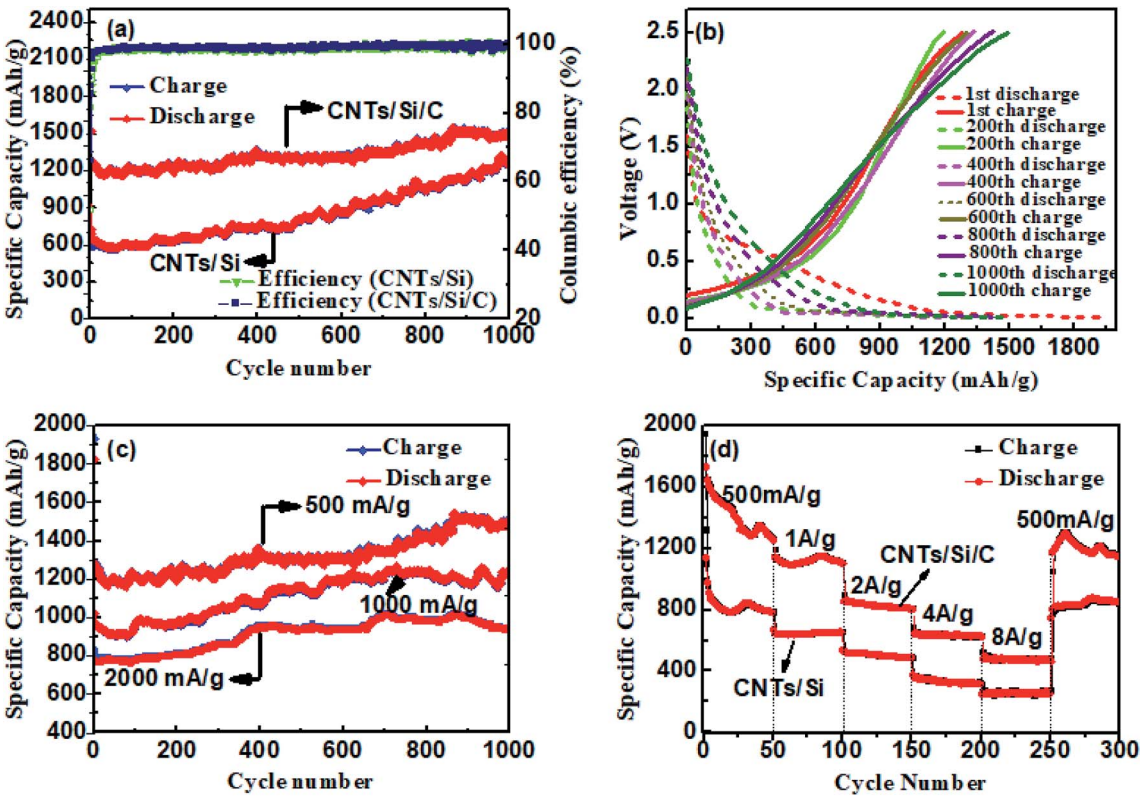

Fig. 4 (a) Cycle performance of cells with prepared anode materials at a current density of 500 mA g^{-1} (green line: efficiency of CNTs/Si; dark blue line: efficiency of CNTs/Si/C), (b) galvanostatic charge–discharge profiles of CNTs/Si/C (solid lines and dashed lines represent the charge and discharge processes, and red, green, magenta, dark yellow, purple and olive corresponds to the 1^{st}, 200^{th}, 400^{th}, 600^{th}, 800^{th} and 1000^{th} cycles, respectively), (c) cycle performance of cells with CNTs/Si/C anodes at different current densities, and (d) rate performance of cells with prepared anode materials.

lower current densities. The gradual increase in capacity may be attributed to the formation of stable polymeric gel layers resulting from kinetically activated electrolyte degradation.[33] These layers could handle repeated absorption and release of lithium ions, resulting in a slight increase in capacity during cycling, as already be reported by several groups.[34,35]

The rate performance of cells assembled with CNTs/Si/C anodes is shown in Fig. 4(d). The discharge capacities of cells with CNTs/Si anodes are 825 mA h g^{-1}, 650 mA h g^{-1}, 517 mA h g^{-1}, 321 mA h g^{-1} and 251 mA h g^{-1}, respectively, with the current densities of 500 mA g^{-1}, 1 A g^{-1}, 2 A g^{-1}, 4 A g^{-1} and 8 A g^{-1}, and when the current density returns to 500 mA g^{-1} after 250 cycles, a discharge capacity of 846 mA h g^{-1} is recovered. After coating a thin carbon layer on the outer Si surface, the rate performance of cells with CNTs/Si/C anodes are greatly improved. The discharge capacities of the cells are 1287 mA h g^{-1}, 1140 mA h g^{-1}, 817 mA h g^{-1}, 636 mA h g^{-1} and 468 mA h g^{-1}, respectively, with the current densities of 500 mA g^{-1}, 1 A g^{-1}, 2 A g^{-1}, 4 A g^{-1} and 8 A g^{-1}, and when the current density goes back to 500 mA g^{-1} after 250 cycles, a discharge capacity of 1168 mA h g^{-1} can be restored. With higher capacitance and stability across all current densities, it is clear that the use of sandwich-like CNTs/Si/C nanotube anodes improves the overall battery performance.

The improved performance can be attributed to the following reasons. First, the mechanical strength of the CNTs and thin carbon layer on both sides of the Si nanotubes can alleviate the impact of the volume change during cycling to stabilize the micro-structure of the anode material. Second, Si nanotubes with thinner walls provide a reduced ion and electron diffusion path during cycling, ensuring better cycling performance at higher current densities. Lastly, the sandwich-like structure of CNTs/Si/C nanotubes reduces the contact area between the electrolyte and Si due to the uniform thin carbon layer and CNTs located on the both sides of Si nanotubes, which enables the formation of a stable SEI layer during the first few cycles. It is found that the sandwich-like CNTs/Si/C possesses a relatively higher coulombic efficiency than the CNTs/Si, indicating that a more stable SEI layer can be formed by coating a thin carbon layer on the surface of CNTs/Si.

Electrochemical impedance spectra (EIS) were recorded to further understand the improved electrochemical performance of sandwich-like CNTs/Si/C, with results summarized in Fig. 5 and Table S1.† The semicircle in the high-medium frequency region in the EIS spectra (Nyquist plots) can be attributed to the charge transfer process at the electrode/electrolyte interface, and an inclined line in the low frequency region describes a typical Warburg behavior, corresponding to the lithium-ion diffusion process in the solid electrodes.[36] The Nyquist plots are fitted with an error value of 0.006 by using the equivalent circuit model.[37] In the equivalent circuit (inset), R_s and R_{ct} are the ohmic resistance and the charge transfer resistance of the electrodes. The constant phase-angle element (CPE) and the Warburg impedance (W) describe the lithium ion diffusion into the anode materials. The numerical value of the diameter of the semicircle gives an approximate indication of the charge transfer resistance (R_{ct}). It is clear that the semicircle in the high-medium frequency region for CNTs/Si/C nanotubes is smaller than that of CNTs/Si, indicating a lower charge transfer resistance of the CNTs/Si/C nanotubes (Fig. 5). According to the fitting results (Table S1†), the R_s, R_{ct} and W of CNTs/Si/C are smaller than those of CNTs/Si, suggesting that the electric conductivity, charge transfer kinetics and diffusion of lithium ions can be effectively improved by forming a sandwich-like structure.

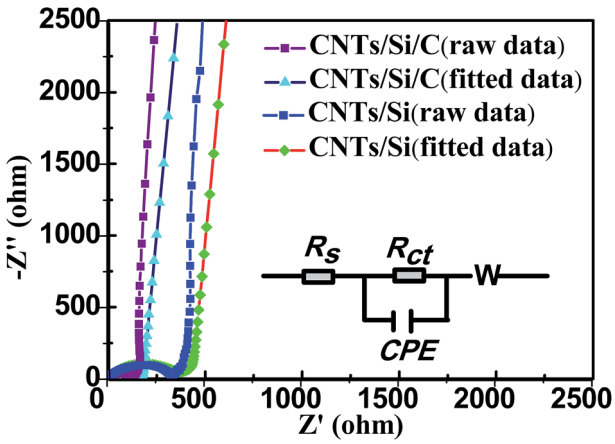

Fig. 5 EIS spectrum of the as obtained CNTs/Si/C and CNTs/Si.

Fig. 6 and S7† show the SEM images and the EDS analysis results, respectively, of the active materials after 1000 cycles by disassembling the cells. It can be seen that the morphologies of the sandwich-like CNTs/Si/C nanotubes remain the same with no evidence of catastrophic pulverization in the electrodes or the silicon nanostructures after over 1000 cycles at current densities of 1000 mA g^{-1}. This indicates that the structures of the Si nanotubes can be preserved during the charge/discharge processes through the addition of an external carbon layer and internal CNTs to effectively encase the Si nanotubes. Although the carbon layer decreases the energy density of the sandwich-like CNTs/Si/C nanotubes, it also improves the surface conductivity and provides mechanical reinforcement to the overall nanostructure, thus reducing capacitance fading in the sandwich-like CNTs/Si/C nanotubes. Moreover, compared to CNTs/Si anode materials, the main function of the thin carbon layer is to isolate the electrolytes and Si nanotubes, which reduces the side reaction between the two components and promotes the formation of stable SEI layer, and thus increasing the utilization of Li.

The improved cycle and rate performance of the sandwich-like CNTs/Si/C can be attributed to several factors (Fig. 7). First, the CNTs/Si/C can increase the contact area between the active materials and electrolytes, allowing lithium ions to intercalate at the interior and exterior of the nanotubes. Second, the carbon layer can stabilize the interface between the Si and electrolytes to promote stable SEI formation and long cycle life. Third, the sandwich-like structures of the CNTs/Si/C can alleviate the volume change during the charge/discharge processes to minimize the formation of cracks and active material delamination from the current collectors. Lastly, both the

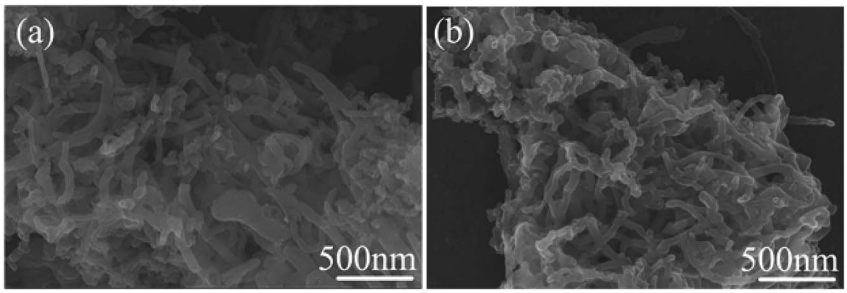

Fig. 6 SEM images of CNTs/Si (a) and CNTs/Si/C (b) after 1000 cycles at a current density of 1000 mA g^{-1}.

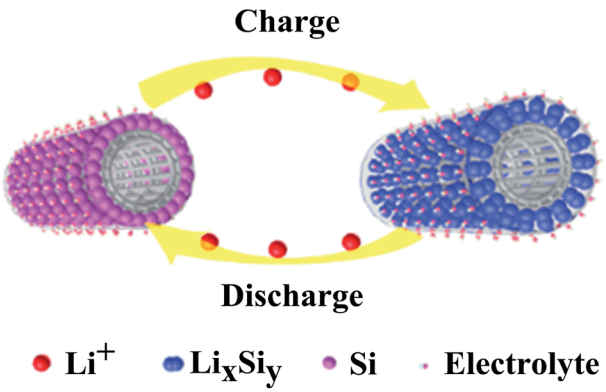

Fig. 7 Schematic diagram of charge and discharge processes within CNTs/Si/C nanotube anodes.

carbon layer and the CNTs can improve the electrical conductivity of the Si nanotubes, which improve lithium intercalation and deintercalation in the Si nanotubes at higher current densities.

Conclusion

Sandwich-like CNTs/Si/C with superior cycle and rate performance have been developed as anode materials for lithium ion batteries. They were successfully prepared by a hydrothermal method followed by magnesiothermic reduction, acid treatment and carbon coating. The improved electrochemical performance of the CNTs/Si/C anode material can be attributed to the sandwich-like hollow tube structure, carbon coating and carbon nanotube reinforcement. All the above characteristics endow the anode materials with improved mechanical resistance, improved electrical conductivity, fast lithium ion diffusion rate and stable electrolyte interface during cycling. These results confirm that the prepared sandwich-like CNTs/Si/C nanotubes are a promising anode material for lithium-ion batteries.

Experimental section

Materials

TEOS, CTAB, ammonia, dopamine hydrochloride, polyvinylidene fluoride (PVDF), $LiPF_6$, ethylene carbonate (EC), diethyl carbonate (DEC), dimethyl carbonate (DMC), HCl and HF were purchased from Sigma-Aldrich. All the reagents are analytically pure. CNTs was purchased from Shenzhen Nanotech Port Company, China. Mg powders were purchased from Shanghai ST-NANO Science & Technology Company, China.

Synthesis of Si/CNTs and CNTs/Si/C

CNTs/Si were synthesized *via* a hydrothermal method using carbon nanotube templates and TEOS as the silicon source, followed by a magnesiothermic reduction process. In a typical synthesis, 1.4 g of CTAB was dissolved in 150 mL of DI-water. Then 18 mL of ammonia was added, followed by 1.8 g of CNTs and 3.5 mL of TEOS to form a homogeneous solution after stirring for 12 h. The solution was transferred into a 100 mL Teflon lined stainless steel autoclave maintained at 100 °C for 72 h. After cooling to room temperature, the samples were collected, washed with DI-water and ethanol three times, and dried at 60 °C overnight under vacuum.

A mixture of 0.5 g of the SiO_2@CNT intermediate and 0.5 g of Mg powders were heated to 750 °C for 4 h under an Ar atmosphere to reduce the SiO_2 to Si. Lastly, the CNTs/Si were treated with diluted HCl and HF under stirring for 12 h to remove remnant MgO and SiO_2, respectively. Pure Si nanotubes can be obtained by heating the CNTs/Si at 650 °C for 4 h.

For preparation of CNTs/Si/C, 300 mg of the as-obtained CNTs/Si were dispersed in Tris solution (50 mL, pH = 8.5) for 1 h to form a uniform suspension, followed by adding 50 mg of dopamine hydrochloride under magnetic stirring at room temperature for 12 h. The resulting precipitates were collected after centrifugation and washed with ethanol and deionized water. The resulting powder was dried at 60 °C for 6 h first and then annealed at 700 °C for 4 h under Ar to convert the polydopamine into carbon.

Characterization method

The morphologies of the samples were characterized by SEM (Zeiss Supra 40 FE) and TEM (JEOL JEM-2100, operated at 200 kV). X-ray diffraction (Bruker D8-Advance diffractometer) was used to determine the phase of the sample. The Raman spectra were recorded on a microscopic confocal Raman spectrometer (Renishaw, RM2000) using 633 nm excitation from an argon ion laser. TG-DSC (Seiko 7300, Japan) was used to determine the carbon content of the composites. X-ray photoelectron

spectroscopy (XPS) (EscaLab 250XI) was used to further identify the chemical state of Si and C in the sample.

Electrochemical characterization

The electrochemical performances of anode materials were evaluated by assembly of CR2032 coin-type cells in a glove box (Mikrouna, Shanghai, China) filled with high purity Ar. The working electrode was made by mixing the CNTs/Si/C, carbon black and polyvinylidene fluoride (PVDF) in a weight ratio of 75 : 15 : 10, and then uniformly spread on Cu foil. Neat lithium metal foil was used as a reference electrode and anode. A microporous polypropylene film (Celgard 2400) was used as a separator, and 1 M $LiPF_6$ dissolved in ethylene carbonate (EC)/diethyl carbonate (DEC)/dimethyl carbonate (DMC) (1 : 1 : 1 by volume) served as the electrolyte. The assembled cells were charged and discharged at different current densities between 0.001 and 3 V at room temperature on a Land 2001A Battery Testing system. The capacity was calculated on the basis of the amount of active materials, and the theoretical capacity of the active materials can be calculated as follows: $C = C_{si} \times V_{si} + C_c \times V_c = 4200 \times 0.7 + 372 \times 0.3 \approx 3052$ mA h g^{-1}. The cyclic voltammograms (CV) were obtained by charging/discharging the cells on an electrochemical workstation (CHI660C, Shanghai Chenhua) at a scan rate of 0.1 mV s^{-1}. The electrochemical impedance spectrum (EIS) was recorded over the frequency range from 100 kHz to 0.01 Hz.

Conflicts of interest

There are no conflicts to declare.

Acknowledgements

The authors acknowledge the financial support from the National Natural Science Foundation of China (NSFC-No. 51202117), the Natural Science Foundation of Beijing (No. 2162037), the Beijing Nova program (Z171100001117077), the Beijing outstanding talent program (No. 2015000020124G121), the Fundamental Research Funds for the Central Universities (No. 2014QJ02), the State Key Laboratory of Coal Resources and Safe Mining (No. SKLCRSM16KFB04), the Key Laboratory of Advanced Materials of Ministry of Education (No. 2018AML03), the Yue Qi Young Scholar Project of China University of Mining & Technology (Beijing) (No. 2017QN17), and the Pengcheng Scholar Program of Shenzhen.

References

1 Y. Li, J. Song and J. Yang, *Renewable Sustainable Energy Rev.*, 2014, **37**, 627–633.
2 Y. Zhao, Y. Ding, Y. T. Li, L. L. Peng, H. R. Byon, J. B. Goodenough and G. H. Yu, *Chem. Soc. Rev.*, 2015, **44**, 7968–7996.
3 M. Armand and J. M. Tarascon, *Nature*, 2008, **451**, 652–657.
4 M. T. McDowell, S. W. Lee, W. D. Nix and Y. Cui, *Adv. Mater.*, 2013, **25**, 4966–4984.
5 B. B. Jiang, C. P. Han, B. Li, Y. J. He and Z. Q. Lin, *ACS Nano*, 2016, **10**, 2728–2735.
6 S. P. Wu, R. Xu, M. J. Lu, R. Y. Ge, J. Iocozzia, C. P. Han, B. B. Jiang and Z. Q. Lin, *Adv. Energy Mater.*, 2015, **21**, 1500400.
7 M. X. Liu, X. M. Ma, L. H. Gan, Z. J. Xu, D. Z. Zhu and L. W. Chen, *J. Mater. Chem. A*, 2014, **2**, 17107–17114.
8 D. A. Agyeman, K. Song, G. H. Lee, M. Park and Y. M. Kang, *Adv. Energy Mater.*, 2016, **28**, 1600904.
9 M. Zhu, J. Yang, Z. H. Yu, H. B. Chen and F. Pan, *J. Mater. Chem. A*, 2017, **5**, 7026–7034.
10 J. Xie, L. Tong, L. W. Su, Y. W. Xu, L. B. Wang and Y. H. Wang, *J. Power Sources*, 2017, **342**, 529–536.
11 Y. Yang, Z. X. Wang, Y. Zhou, H. J. Guo and X. H. Li, *Mater. Lett.*, 2017, **199**, 84–87.
12 Y. H. Ma, H. Q. Tang, Y. Zhang, Z. F. Li, X. H. Zhang and Z. Y. Tang, *J. Alloys Compd.*, 2017, **704**, 599–606.
13 B. B. Deng, L. Shen, Y. A. Liu, T. Yang, M. S. Zhang, R. J. Liu, Z. H. Huang, M. H. Fang and X. W. Wu, *Chin. Chem. Lett.*, 2017, **28**, 2281–2284.
14 C. C. Fang, Y. F. Deng, Y. Xie, J. Y. Su and G. H. Chen, *J. Phys. Chem. C*, 2015, **119**, 1720–1728.
15 D. T. Ngo, H. T. T. Le, X. M. Pham, J. W. Jung, N. H. Vu, J. G. Fisher, W. B. Im, I. D. Kim and C. J. Park, *J. Mater. Chem. A*, 2018, **6**, 2834–2846.
16 T. Shen, X. H. Xia, D. Xie, Z. J. Yao, Y. Zhong, J. Y. Zhan, D. H. Wang, J. B. Wu, X. L. Wang and J. P. Tu, *J. Mater. Chem. A*, 2017, **5**, 11197–11203.
17 J. Bae, D. S. Kim, H. Yoo, E. Park, Y. G. Lim, M. S. Park, Y. J. Kim and H. Kim, *ACS Appl. Mater. Interfaces*, 2016, **8**, 4541–4547.
18 X. M. Ma, M. X. Liu, L. H. Gan, P. K. Tripathi, Y. H. Zhao, D. Z. Zhu, Z. J. Xu and L. W. Chen, *Phys. Chem. Chem. Phys.*, 2014, **16**, 4135–4142.
19 M. T. McDowell, S. W. Lee, I. Ryu, H. Wu, W. D. Nix, J. W. Choi and Y. Cui, *Nano Lett.*, 2011, **11**, 4018–4025.
20 T. Song, J. L. Xia, J. H. Lee, D. H. Lee, M. S. Kwon, J. M. Choi, J. Wu, S. K. Doo, H. Chang, W. Il Park, D. S. Zang, H. Kim, Y. G. Huang, K. C. Hwang, J. A. Rogers and U. Paik, *Nano Lett.*, 2010, **10**, 1710–1716.
21 T. Song, Y. Jeon and U. Paik, *J. Electroceram.*, 2014, **32**, 66–71.
22 D. Gueon, D. Y. Kang, J. S. Kim, T. Y. Kim, J. K. Lee and J. H. Moon, *J. Mater. Chem. A*, 2015, **3**, 23684–23689.
23 F. Gunes, *RSC Adv.*, 2016, **6**, 1678–1685.
24 Y. F. Chen, N. Du, H. Zhang and D. R. Yang, *CrystEngComm*, 2017, **19**, 1220–1229.
25 B. Gattu, R. Epur, P. H. Jampani, R. Kuruba, M. K. Datta and P. N. Kumta, *J. Phys. Chem. C*, 2017, **121**, 9662–9671.
26 B. S. Chen, Q. L. Xu, X. L. Zhao, X. G. Zhu, M. G. Kong and G. W. Meng, *Adv. Funct. Mater.*, 2010, **20**, 3791–3796.
27 Y. F. Chen, N. Du, H. Zhang and D. R. Yang, *J. Alloys Compd.*, 2015, **622**, 966–972.
28 W. S. Kim, J. Choi and S. H. Hong, *Nano Res.*, 2016, **9**, 2174–2181.
29 L. Miao, D. Z. Zhu, M. X. Liu, H. Duan, Z. W. Wang, Y. K. Lv, W. Xiong, Q. J. Zhu, L. C. Li, X. L. Chai and L. H. Gan, *Electrochim. Acta*, 2018, **274**, 378–388.

30 D. Zhu, J. Jiang, D. Sun, X. Qian, Y. Wang, L. Li, Z. Wang, X. Chai, L. Gan and M. Liu, *J. Mater. Chem. A*, 2018, **6**, 12334–12343.
31 C. F. Liu, C. K. Zhang, H. Y. Fu, X. H. Nan and G. Z. Cao, *Adv. Energy Mater.*, 2017, **7**, 1601127.
32 M. Haro, V. Singh, S. Steinhauer, E. Toulkeridou, P. Grammatikopoulos and M. Sowwan, *Adv. Sci.*, 2017, **4**, 1700180.
33 X. W. Li, L. Qiao, D. Li, X. H. Wang, W. H. Xie and D. Y. He, *J. Mater. Chem. A*, 2013, **1**, 6400–6406.
34 J. S. Luo, J. L. Liu, Z. Y. Zeng, C. F. Ng, L. J. Ma, H. Zhang, J. Y. Lin, Z. X. Shen and H. J. Fan, *Nano Lett.*, 2013, **13**, 6136–6143.
35 W. Wei, S. B. Yang, H. X. Zhou, I. Lieberwirth, X. L. Feng and K. Mullen, *Adv. Mater.*, 2013, **25**, 2909–2914.
36 C. P. Han, D. Yang, Y. K. Yang, B. B. Jiang, Y. J. He, M. Y. Wang, A. Y. Song, Y. B. He, B. H. Li and Z. Q. Lin, *J. Mater. Chem. A*, 2015, **3**, 13340–13349.
37 T. Xia, W. Zhang, Z. H. Wang, Y. L. Zhang, X. Y. Song, J. Murowchick, V. Battaglia, G. Liu and X. B. Chen, *Nano Energy*, 2014, **6**, 109–118.